

# The AMAP Climate and Air Quality Emulator

Technical summary

Knut von Salzen, Canadian Centre for Climate Modelling and Analysis, Victoria, BC, Canada

Email: knut.vonsalzen@ec.gc.ca

Nov 22, 2021

## *Introduction*

Climate forcings can have very different abilities to affect climate, depending on the time scale of climate impacts. Global atmospheric lifetimes of important climate forcings range from days (for aerosols and other short-lived climate forcings, SLCFs) to centuries (for greenhouse gases such as CO<sub>2</sub>). The efficiency to scatter or absorb radiation of gases and aerosols can differ greatly, which further affects the spatio-temporal patterns and magnitude of climate impacts. In addition, air quality impacts of climate forcings vary in the atmosphere, owing to differences in atmospheric processes.

Given the large differences in greenhouse gas and aerosol lifetimes and interactions with climate and air quality, it can be challenging to compare their impacts globally. It is even more challenging to assess regional impacts, e.g. aerosol climate processes vary regionally, depending on aerosol interactions with local snow or cloud cover.

In addition, unforced climate process variability, e.g. “weather noise”, needs to be considered. For instance, simulated temperature impacts of a climate forcing emitted from a relatively clean source are more strongly obscured by temperature variability than emissions from a heavily polluting source, especially in model projections of near-term climate trends, i.e. over several years to a few decades. This raises questions about the statistical robustness of diagnosed climate impacts.

To address these various challenges efficiently, a range of different models is needed. Complex Earth System Models (ESMs) simulate highly complex air pollutant and radiative forcing processes. However, the high computing costs of these models and considerable model uncertainties (e.g., in climate feedbacks and parameterizations of SLCF processes) substantially limit their usefulness for assessments of the climate and air quality impacts where emissions of multiple pollutants from different sources need to be considered. Consequently, multi-model assessment of SLCFs with these models have focussed on changes in global climate forcing emissions. Statistically robust radiative forcings from interactions of different aerosol species with clouds or snow are often lacking, especially at regional scales. For these reasons, ESM-based scenarios alone may not be suitable for the development of mitigation policies targeting multiple climate forcings that are emitted from different sources.

In contrast to ESMs, climate emulators are highly approximated models for rapid assessments of the impacts of emission changes on radiative forcings and temperature. In addition, air quality source-receptor models are used to assess air quality responses to emission changes. Climate emulators and air quality source-receptor models employ analytic relationships between emissions, concentrations, or radiative forcing. These models are numerically inexpensive because the net concentration and forcing impacts of numerous complex physical and chemical processes are highly parameterized. The parameterizations are either directly based on results from ESMs or air quality grid point models, or

they are tuned to match results from more sophisticated models or multi-model ensembles. Given the simplicity of the parameterizations, climate emulators cannot be used to simulate changes in sea ice, precipitation, or other important climate variables. Further, unforced inter-annual to multi-decadal climate variability is not simulated.

Despite the simplicity of climate emulators, forced temperature trends simulated by climate and ESMs have been reproduced to within the uncertainty of the ESM simulations, across a wide range of scenarios (Meinshausen et al., 2011; Good et al., 2011, 2013; Geoffroy et al., 2013; Smith et al., 2018; Forster et al., 2020; Tsutsui, 2020). Similar, source–receptor air quality models have been successfully used to simulate impacts of emissions on air quality (Alcamo et al., 1995, Heyes et al., 2011; Foley et al., 2014; Li et al., 2014; Liu et al., 2017; Porter et al., 2017; van Dingenen et al., 2018).

Here, a new combined climate and air quality emulator is summarized for simulating linkages between emissions, climate, and air quality. Annual mean emissions of CO<sub>2</sub>, CH<sub>4</sub>, CO, NO<sub>x</sub>, VOC, sulfur, black carbon (BC), and organic carbon (OC) are used. No other climate forcers are considered, which implies that simulated warming trends are likely underestimated although this should not affect the comparisons in this study. Climate and air quality impacts of emissions from 7 different regions are simulated: Western Arctic Council (Canada and United States), Eastern Arctic Council (Kingdom of Denmark, Finland, Iceland, Norway, the Russian Federation, and Sweden), Rest of Europe, Arctic Council Asian Observer countries (Japan, People’s Republic of China, Republic of India, Republic of Korea, Republic of Singapore), and the Rest of the World. Results for climate forcing processes and their uncertainties are also available from the emulator simulations.

The following sections summarize the underlying mathematical concepts, their key features and limitations. Further details are available in AMAP (2021).

### *Air quality response to emission changes*

The emulator simulations of air pollutant concentrations are based on pre-calculated linear relationships between regional emissions and concentration responses from simulations with 3D grid-point models. Source–receptor relationships are used to simulate impacts of emissions on annual mean air pollutant concentrations. Similar to the climate emulator component, efficiency of calculations is achieved through a rigorous linearization of complex physical and chemical atmospheric processes. This can limit the accuracy of simulated concentration responses involving non-linear processes (e.g. Yang et al., 2019).

Emissions,  $E_p(t)$  (in kg/year), of sulfur, BC, and OC are linked to speciated near-surface PM<sub>2.5</sub> concentrations,  $C$  (in kg m<sup>-3</sup>), in the emulator, which are spatially and annually varying. The parameterized source-receptor relationships are based on the assumption that atmospheric lifetimes of the emitted species are short, i.e.  $\tau_i \ll 1$  yr, so that a linear relationship between annual mean emissions and concentrations can be used as an approximation, i.e.

$$C(\mathbf{x}, t) = \sum_{p=1}^P c_p(\mathbf{x}) \left( E_p(t) - E_p(t_{ref}) \right) .$$

Here,  $c_p(\mathbf{x})$  are spatially variable concentration sensitivities, which were determined by perturbing emissions in comprehensive 3D models for source or region  $p$  and recording the equilibrated response in simulated PM<sub>2.5</sub> concentration to that perturbation, i.e. relative to the reference year  $t_{ref}= 2015$ ,

$$c_p = \frac{dC}{dE_p} .$$

Downscaled multi-model mean results from CanAM5-PAM, CESM2.0, MRI-ESM2, and UKESM1, are used, as described in more detail below. In addition,  $PM_{2.5}$  background concentrations,  $C_0(x)$ , are specified to account for contributions from sea salt and mineral dust aerosols, which are assumed to be steady.

In order to better reproduce concentration gradients for the analysis of health impacts we first downscale the  $PM_{2.5}$  concentrations that are simulated in the 3D models to derive concentration sensitivities and further conduct the air quality analysis at a resolution of  $0.5^\circ$  latitude and longitude. This means that we effectively increase the horizontal resolution of the 3D model results by scaling these linearly using a global, non-Arctic satellite-based dataset from Dalhousie University at a resolution of  $0.5^\circ$  ([http://fizz.phys.dal.ca/~atmos/martin/?page\\_id=140](http://fizz.phys.dal.ca/~atmos/martin/?page_id=140), van Donkelaar et al., 2016). The overall goal is to enhance regional  $PM_{2.5}$  concentration patterns by introducing spatial  $PM_{2.5}$  variability at scales that are unresolved by the model but are important for health impacts. By design, the approach preserves the large-scale features that are resolved by the models at their native resolution.

The approach described above is used for different source sectors in each region. Different values of  $c_p(x)$  are available for emissions from upstream oil and gas production sources (“oil & gas flaring”) and combined fossil and bio fuel sources related to energy consumption (“fossil & bio fuel”). The former includes storage and distribution, including the intended venting and unintended leakage during extraction and transportation of oil and gas, the release of ventilation air  $CH_4$  during coal mining, and the flaring of excess gases and liquids. The latter includes land-based emissions from residential and commercial sources; agriculture and waste burning on fields; power plants, energy conversion and extraction; industrial combustion and processing; surface transportation; and waste processing. In addition to these upstream and downstream sources, emissions from international shipping sources (“shipping”) are considered as a separate emission source, too.

### *Climate response to emission changes*

The response of climate to emission changes in the emulator is simulated based on linearized and highly approximated mass and energy balances of the climate system. Consistent with the approach for near-surface  $PM_{2.5}$  described above, linear relationships between emissions in 5 regions and radiative forcings are assumed, for 3 separate source categories.

Conceptually, the emulator simulates the forced response in the global and Arctic mean surface air temperatures to a series of instantaneous pulse emissions of different chemical species, which affect the energy balance of the climate system by changing radiative forcings of greenhouse gases and SLCFs. The temporal evolution of the regional mean temperature in response to the pulse emission is approximated using a specified climate sensitivity, time scales of heat dissipation, and other parameters derived from simulations with more comprehensive models, in addition to Regional Temperature-Change Potentials, which were previously used for the AMAP 2015 black carbon and ozone assessment (AMAP, 2015). Furthermore, radiative forcings of  $CO_2$  and  $CH_4$  are simulated, based on global atmospheric mass budgets which account for key physical and chemical loss processes.

To compare impacts of emissions of different greenhouse gases on global mean temperature, Shine et al. (2005) proposed the Global Temperature Change Potential (GTP) as a metric, based on a linearized energy budget of the global climate system (e.g. Roe, 2009). As an extension of this

approach, Boucher and Reddy (2008) and Fuglestedt et al. (2010) subsequently introduced the Absolute Global Temperature-Change Potential (AGTP) to determine the surface temperature response following an instantaneous pulse emission of a well-mixed greenhouse gas or short-lived climate forcer, which can be defined as

$$AGTP(H) = \int_0^H A(t) R(H-t) dt, \quad (1)$$

where the units are  $K \text{ kg}^{-1}$  and  $H$  is the annual time horizon (in yr), which represents the time elapsed between the times of the pulse emission and temperature response. The two terms in the integral on the right hand side of Eq. (1) represent the radiative forcing of the climate forcer and temperature response to the radiative forcing, respectively, as described below.

In addition to global temperature impacts, regional temperatures impacts are approximated, based on the Absolute Regional Temperature-Change Potential (ARTP; Shindell and Faluvegi, 2009; Shindell and Faluvegi, 2010; Shindell, 2012, Collins et al., 2013). As an extension of the AGTP concept, the emulator additionally accounts for the transport of heat between the different regions of the earth system. Specifically, it provides the temperature response in region  $m$  to a radiative forcing in region  $l$ , where  $l, m = 1, \dots, M$ , for a total of  $M$  separate regions. Similar to the approach which was first used by Shindell and Faluvegi (2009),  $M = 4$  is used in the emulator, for latitude bands from  $60^\circ\text{N}$  to  $90^\circ\text{N}$  (Arctic),  $28^\circ\text{N}$  to  $60^\circ\text{N}$  (northern hemispheric mid-latitudes),  $28^\circ\text{S}$  to  $28^\circ\text{S}$  (tropics), and  $90^\circ\text{S}$  to  $28^\circ\text{S}$  (southern hemisphere mid-latitudes and Antarctica).

A linear decomposition of the temperature responds to a pulse emission yields (in  $K \text{ kg}^{-1}$ )

$$ARTP_m(H) = AGTP(H) g \left( \frac{1}{\lambda \delta F_0} \right) RTP_m, \quad (2)$$

with the Regional Temperature-Change Potential (RTP) in region  $m$  (in K),

$$RTP_m = \sum_{l=1}^M k_{lm} \delta F_{0l},$$

where  $\delta F_{0l}$  is the radiative forcing perturbation in region  $l$  (in  $\text{W m}^{-2}$ ), which is associated with the pulse emission at  $t = 0$  (e.g. Collins et al., 2013). A summation of the regional forcings yields the global radiative forcing perturbation,  $\delta F_0 = \delta F_{01} + \dots + \delta F_{0M}$ . Further,  $\lambda$  is the equilibrium climate sensitivity parameter (in  $\text{K (W m}^{-2}\text{)}^{-1}$ ; Roe, 2009) and  $k_{lm}$  is a matrix of regional temperature response coefficients (in  $\text{K (W m}^{-2}\text{)}^{-1}$ ). These and the dimensionless scaling factor  $g$  in Eq. (2) are described below.

$RTP_m$  in Eq. (2) approximates the equilibrated temperature response to a steady forcing. The temperature response coefficients used here were obtained from simulations with the coupled atmosphere–ocean climate model GISS-ER (Shindell and Faluvegi, 2009). They were derived for different types of climate forcings and are applied to different forcing processes in the emulator, similar to the approach that was previously used for the AMAP black carbon and ozone assessment in 2015 (AMAP, 2015).

The term in the brackets on the right hand side of Eq. (2) ensures that the equilibrium climate sensitivity,  $ECS = \lambda F_{2x}$  (in K), matches the climate sensitivity as implied by the globally integrated RTP, i.e.

$$ECS_{RTP} = \frac{F_{2x}}{\delta F_0} \sum_m \sum_l k_{lm} \delta F_{0l} z_m ,$$

with the global radiative forcing from doubling of  $CO_2$ ,  $F_{2x}$ , and the global area fraction of region  $m$ ,  $z_m$  (in  $m^2 m^{-2}$ ).

In order to ensure that the emulator is sufficiently constrained by results from comprehensive 3D models, the climate sensitivity in the emulator needs to be consistent with the climate sensitivity produced by these models. GISS-ER produces a lower equilibrium climate sensitivity than that derived from results of ESM simulations in Phase 6 of the Coupled Model Intercomparison Project, CMIP6 (i.e. approx. 2.7 vs 3.7 K; Schmidt et al., 2006; Meehl et al., 2020; Nijssse et al., 2020; Zelinka et al., 2020). Therefore the ARTP is scaled so that the ARTP-implied equilibrium climate sensitivity matches the specified climate sensitivity, consistent with the AGTP and  $\lambda$ . This is accomplished by scaling results of Eq. (2) by a factor

$$g = \frac{\lambda F_{2x}}{ECS_{RTP}} . \quad (3)$$

Subsequently, Eq. (2) is used to calculate the forced response of regional temperatures to time-varying emissions by representing the annual mean emissions as a series of pulse emissions. This leads to a series of ARTPs with annually varying time horizons, which are added up to approximate the forced net regional temperature response in region  $m$  to specified annual mean emissions over  $N$  number of years, starting with year  $t_0$ , i.e.

$$T_m(t + \delta t_0) - T_{0m}(t + \delta t_0) = \sum_{n=0}^N U(t - t_0 - n\delta t_0) ARTP_m(t - t_0 - n\delta t_0) E(t_0 + n\delta t_0) \delta t_0 ,$$

where  $T_{0m}(t + \delta t_0)$  is the regional temperature in the baseline scenario, which does not include the forced temperature response to the specified emissions, e.g. the temperature in an unforced control simulation. For sake of simplicity, a time scale of  $\delta t_0 = 1$  yr is used to represent pulse emissions in the emulator, which facilitates the use of annual mean emissions in the following, without notable impacts on numerical solutions of Eq. (1). Further,  $U(t)$  is the Heaviside step function,

$$U(t) = \begin{cases} 0 & , t < 0 \\ \frac{1}{2} & , t = 0 \\ 1 & , t > 0 \end{cases} .$$

The high degree of linearization of the temperature response implies that simulation results are most accurate close to the reference (baseline) year, within the time period of interest of the emulator simulations. For simulations discussed here, the reference year is  $t_{ref} = 2015$  and the total time period of interest is from 1990 to 2050, with a focus of the analysis on the time period from 1990 to 2030. Further, the emulator simulations are initialized in 1990 based on results from a spin-up emulator simulation for the time period from 1850 and 1990, with historical emissions used for simulations with CMIP6 models.

By extension, the net temperature response to emissions of multiple chemical species from different sources and regions are obtained by superimposing forced temperature changes, based on the appropriate radiative forcings and temperature response coefficients in the ARTPs for the different climate forcers.

In the following sections, terms in the equations governing the temperature responses (Eqs. 1 and 2) will be described in more detail.

### *Global radiative forcing efficiency*

$A(t)$  in Eq. (1) is the radiative forcing efficiency of the climate forcer, defined here as

$$A(t) = \frac{\epsilon \delta F(t)}{\delta E \delta t_0}, \quad (4)$$

where  $\delta E \delta t_0$  is the global and annual mean abundance of the climate forcer in the atmosphere immediately following a pulse emission,  $\delta E$  (in kg/yr), at time  $t = 0$ .  $\epsilon$  is the efficacy of the climate forcer (Hansen et al., 2005).

Further,  $\delta F(t)$  is the time-evolving global radiative forcing perturbation (in  $\text{W m}^{-2}$ ), which is associated with the pulse emission, as described below.

### *Global temperature response*

The term  $R(H - t)$  in Eq. (1) gives the surface temperature perturbation at the time horizon  $H$  in response to the radiative forcing. We closely follow the approach proposed by Boucher and Reddy (2008) and use a temperature response function to represent the forcing impact on the climate system of the form

$$R(t) = \sum_{j=1}^2 \frac{c_j}{d_j} \exp\left(-\frac{t}{d_j}\right),$$

where the coefficients  $c_1 = 0.595 \text{ K (W m}^{-2}\text{)}^{-1}$ ,  $c_2 = 0.405 \text{ K (W m}^{-2}\text{)}^{-1}$  are climate sensitivity parameters and  $d_1 = 8.4 \text{ yr}$ ,  $d_2 = 409.5 \text{ yr}$  are temperature response time scales (Boucher and Reddy, 2008; Shindell and Faluvegi, 2010). Physically, the first term in the summation approximates the temperature response in the ocean mixed-layer and the second term the slower response of the deep ocean, as simulated in ESMs.

With the parameter choices described above, the emulator equilibrium climate sensitivity is about 10% higher than the value that was used by Shindell and Faluvegi (2010), owing to the relatively low GISS-ER equilibrium climate sensitivity, as described above. As can be derived from Eq. (1), the equilibrium climate sensitivity parameter is given by  $\lambda = c_1 + c_2 = 1.0 \text{ K (W m}^{-2}\text{)}^{-1}$ , which matches multi-model mean results from CMIP6 models, i.e.  $\lambda = \text{ECS}/F_x = 3.7 \text{ K}/3.7 \text{ W m}^{-2}$ . In general, the climate sensitivity of the earth system is uncertain and considerable differences between model-based estimates and transient climate sensitivity exist (Sherwood et al., 2020). Additional simulations with modified values of  $\lambda$  were conducted with the emulator to determine how these affect temperature uncertainties.

While the scientific understanding of the climate sensitivity of the global earth system is steadily evolving, changes in regional temperatures are much less well understood. There is not enough data available to quantify uncertainties in Arctic amplification and regional energy budgets. Therefore, we have less confidence in the Arctic than the global temperature changes simulated by the emulator.

### *Response of climate forcer global abundances and near-surface concentrations*

In order to relate emission changes to the radiative forcing in Eq. (4), it is useful to first consider the impacts of emissions on the abundances of the climate forcers.

For emissions of any atmospheric climate forcer or air pollutant, impacts on climate or air quality decay over time as chemical or deposition processes may start to deplete the climate forcer soon after emission into the atmosphere. It is assumed that the temporal evolution of the global abundance of the climate forcer or air pollutant,  $B(t)$ , can be approximated by assuming temporally varying global emissions,  $E(t)$ , and a series of exponential decay processes, i.e.

$$B(t) = B_0 + \sum_{i=1}^I B_i(t),$$

with

$$\frac{d B_i}{d t} = -\frac{1}{\tau_i} B_i + a_i E(t),$$

which yields the following solution, following a pulse emission at  $t = 0$ ,

$$B(t) = B_0 + \delta E \delta t_0 \sum_{i=1}^I a_i \exp\left(-\frac{t}{\tau_i}\right),$$

where  $\tau_i$  denotes the time scale of atmospheric removal by process  $i = 1, \dots, I$  and  $a_i$  refers to constant fractions of emissions, with  $a_1 + \dots + a_I = 1$ .  $B_0$  refers to an equilibrated background state due to specified processes and emissions, which is used to account for impacts of preindustrial emissions in emulator simulations of the impact of anthropogenic emissions on climate forcer or air pollutant abundance.

### *Radiative forcing response*

The global radiative forcing perturbation of a general climate forcer (Eq. 4) is approximated by assuming a linear relationship between radiative flux perturbations and climate forcer abundance. Following the approach for the simulation of abundance changes, this yields

$$\delta F(t) = \delta F_0 \sum_{i=1}^I a_i \exp\left(-\frac{t}{\tau_i}\right),$$

during the time period following the pulse emission. Note that this approach is based on the simplifying assumption of a linear response of the radiative forcing perturbation to concentration changes. If the emission pulses are sufficiently small then the approach can be used to approximate non-linear responses of radiative forcings to abundance changes, i.e. by calculating  $\delta F_0$  as a function of the unperturbed abundance from before the emission pulse.

For short-lived climate forcers with  $\tau_i \ll H$ , radiative forcings are a linear function of emissions, provided that linear relationships exist between climate forcer abundance and emissions and between radiative flux perturbations and abundance, as assumed above. Hence,

$$\delta F(x, t) = \sum_{p=1}^P f_p(x) E_p(t),$$

with radiative forcing sensitivities,

$$f_p = \frac{dF}{dE_p},$$

derived from 3D model simulations with perturbed emissions, relative to the baseline case with emissions and meteorological conditions in 2015. Subsequently, spatially variable radiative forcings are integrated to obtain global radiative forcings (for calculations of AGTPs) and regional mean forcings (for calculations of ARTPs), where  $\delta F_{0l}$  is obtained by integrating  $\delta F(x, t)$  over each latitude band and selecting the time of the pulse emission ( $t = 0$ ). Multi-model mean results from simulations with CanAM5-PAM, MRI-ESM2, and UKESM1 with specified sea-surface temperatures for 2015 are used in the emulator.

Similar, separate radiative forcings and ARTPs are obtained for emissions from different regions, sectors, and for different forcing processes by calculating the corresponding forcing sensitivities, based on 3D climate model simulations with regionally perturbed SLCF sources.

The assumption of linearity of the radiative forcing considerably simplifies calculations of AGTPs for aerosols and ozone (Fuglestedt et al., 2010), including for secondary climate forcers and air pollutants. For example, methane and ozone abundances are coupled through hydroxyl radical oxidation processes. In detail, the ozone radiative forcing depends on the rate of methane oxidation. Vice versa, the methane oxidation rate depends on ozone precursor emissions. Methods for including the combined effects of ozone precursor emissions and oxidation on radiative forcings are summarized below.

### *Regional equilibrium temperature change*

In order to complete the summary of the model framework described in previous sections, it is necessary to quantify the relationship between regional radiative forcings and equilibrium temperature change for the RTP in Eq. (2). In order to calculate the RTP and solve this equation, regional temperature response coefficients are needed, which are given in Table S1.

Effective radiative forcings are used in the emulator in order to account for interactions of aerosols with radiation, surface albedo, and clouds (Ghan, 2013; Forster et al., 2016). In contrast to direct radiative forcings (which are also available in the emulator), effective radiative forcings additionally account for impacts of rapid physical feedbacks on radiative transfer, which are semi-directly or indirectly associated with SLCF concentration changes. For instance, this includes responses in amounts and optical properties of clouds and snow, which can have substantial impacts on atmospheric radiative fluxes and climate.

Rapid feedback processes are usually small in calculations of temperature responses from interactions of aerosols with radiation in the atmosphere, compared to other forcing processes. Consequently, it is assumed that the same temperature response coefficients can be used for interactions of aerosol species with radiation for direct and effective radiative forcing calculations.

Climate model simulations provide evidence for strong feedbacks of the surface albedo to absorption of solar radiation by black carbon in snow. The associated effective radiative forcing is larger than the direct surface albedo forcing from the absorption of solar radiation by black carbon in snow. Consequently, the efficacy of the black carbon surface albedo forcing is greater than unity (Hansen et al., 2005). Here it is assumed that the temperature response coefficients are similar to those for interactions of black carbon with radiation in the atmosphere.

Temperature responses to interactions of aerosol species with clouds are simulated using the same regional temperature response coefficients as for interactions of scattering aerosol species, given that the scattering of solar radiation is a key contributor to both of these forcing processes and the efficacy

of scattering aerosols is close to unity (Hansen et al., 2005). Note that indirect and semi-direct effects of aerosols in clouds contribute to simulated temperature responses owing to the use of effective radiative forcings in the emulator.

The local near-surface temperature response to black carbon forcing in the Arctic and elsewhere depends strongly on the altitude the radiative heating of the air by black carbon absorption of solar radiation (Ban-Weiss et al., 2011; Flanner, 2013; Sand et al., 2013). Similar to the AMAP (2015), a technique was devised to derive vertically-resolved black carbon radiative forcings and apply these in combination with vertically varying temperature response coefficients in the Arctic. This leads to variable regional temperature response coefficients for interactions of black carbon with radiation in the Arctic atmosphere (Table S1), as discussed below.

As an improvement over the technique that was used before (AMAP, 2015), local equilibrium Arctic temperature changes are determined based on an annual mean vertically-resolved Arctic black carbon effective radiative layer forcing,  $\delta\hat{F}_{0y}$ , with layer index  $y$  and units of  $W\ m^{-2}\ hPa^{-1}$ . These are multiplied by vertically varying Arctic temperature response coefficients  $\hat{k}_y$  (Table S2) and layer depth  $\Delta p_y$  (in hPa) to obtain the local equilibrium near-surface air temperature in response to the Arctic forcing, i.e.

$$\delta\hat{T}_0 = \sum_{y=1}^{16} \hat{k}_y \delta\hat{F}_{0y} \Delta p_y .$$

The values of  $\hat{k}_y$  in Table S2 are based on the simulated responses of Arctic temperatures to specified Arctic black carbon concentration perturbations in the Community Earth System Model (CESM; Flanner, 2013). Specifically, the simulated equilibrium temperature changes in response to separate black carbon concentration perturbations in 5 different layers were divided by the differences between corresponding top-of-atmosphere and surface radiative forcings (Table 1 in Flanner, 2013). Subsequently, a curve fitting procedure was applied to generate the coefficients in Table S2.

In practice,  $\delta\hat{F}_{0y}$  can be determined by calculating effective radiative forcings for different layers of the atmosphere in a climate model, as an extension of the calculation of effective radiative forcings at the top-of-atmosphere according to Ghan (2013). However, an alternative approach is to approximate  $\delta\hat{F}_{0y}$  by vertically integrating annual mean concentrations of black carbon over different layers of the Arctic atmosphere and to scale these by the simulated top-of-atmosphere effective radiative forcing and specified radiative efficiency profiles, which can be obtained from additional model simulations, if necessary. Here, monthly radiative efficiency profiles from simulations with CanAM5-PAM were used in combination with monthly black carbon layer burdens from CESM2 and MRI-ESM2 to approximate  $\delta\hat{F}_{0y}$  for these two models.

Simulated results for  $\delta\hat{T}_0$  for CanAM5-PAM agree well with results based on the technique which was previously used by AMAP (2015). In contrast to the latter, the technique outlined above has the advantage that it provides a more straightforward approach which avoids assumptions concerning the radiative efficiency of black carbon concentration perturbations.

Finally, the regional temperature response coefficient for interactions of black carbon with radiation in the Arctic (Eq. 2 and Table S1) is determined as the ratio of the local Arctic temperature response over the Arctic top-of-atmosphere black carbon effective radiative forcing, i.e.

$$k_{11} = \frac{\delta \hat{T}_0}{\delta F_{01}} ,$$

which may be negative or positive, depending on the vertical profiles of black carbon concentrations in the Arctic.

### Carbon dioxide

The model framework described above is used for simulations of changes in global CO<sub>2</sub> abundance in response to CO<sub>2</sub> emissions in the emulator. The uptake of CO<sub>2</sub> by the ocean and terrestrial sinks involves complex processes which can be simulated in comprehensive ESMs and other 3D grid-point models. Millar et al. (2017) approximated the complexity of the global carbon cycle dynamic by simulating anomalies in global atmospheric CO<sub>2</sub> abundance, relative to preindustrial conditions, in four separate “carbon reservoirs”, i.e.

$$\frac{d B_{\text{CO}_2,i}}{dt} = -\frac{1}{\tau_{\text{CO}_2,i}} B_{\text{CO}_2,i} + a_i E_{\text{CO}_2} ,$$

where  $B_{\text{CO}_2,i}$  denotes the anomaly in global atmospheric CO<sub>2</sub> abundance (in kg) in reservoir  $i$ , with  $i = 1, \dots, 4$ , and  $E_{\text{CO}_2}$  represents emissions of CO<sub>2</sub>, similar to the approach by Myhre et al. (2013). Time scales,  $\tau_{\text{CO}_2,i}$ , and fractions of emissions into each reservoir,  $a_i$ , are given in Table S3. For simulations with the emulator, this approach is applied separately to emissions from different regions in order to determine regional contributions to the total CO<sub>2</sub> abundance from all sources,  $B_{\text{CO}_2}$ .

The radiative forcing efficiency of CO<sub>2</sub> is given by

$$A(t) = A_0 \sum_{i=1}^4 a_i \exp\left(-\frac{t}{\tau_{\text{CO}_2,i}}\right) ,$$

with an initial radiative forcing efficiency, immediately following the pulse emission of CO<sub>2</sub>,

$$A_0 = \frac{\delta F_0}{\delta B_{\text{CO}_2}} ,$$

which is obtained by evaluating the sensitivity of the effective CO<sub>2</sub> radiative forcing ( $F_0$ ) to a small perturbation in CO<sub>2</sub> abundance ( $B_{\text{CO}_2}$ ), assuming an efficacy of  $\epsilon = 1$ . The global effective CO<sub>2</sub> radiative forcing is calculated following Etminan et al. (2016), using the total simulated CO<sub>2</sub> abundance change, which is added to a pre-industrial CO<sub>2</sub> abundance of 284.3 ppm. In addition, a N<sub>2</sub>O abundance of 323 ppb (Meinshausen et al., 2017) is assumed for the calculation of the effective CO<sub>2</sub> radiative forcing according to Etminan et al. (2016).

Consequently, the Absolute Global Temperature-Change Potential of CO<sub>2</sub> (Eq. 1) is given by

$$\text{AGTP}(H) = A_0 \sum_{i=1}^4 \sum_{j=1}^2 \frac{a_i \tau_{\text{CO}_2,i} c_j}{\tau_{\text{CO}_2,i} - d_j} \left[ \exp\left(-\frac{H}{\tau_{\text{CO}_2,i}}\right) - \exp\left(-\frac{H}{d_j}\right) \right]$$

and the ARTP of CO<sub>2</sub> is given by Eq. (2), with no distinction between regional and global radiative forcing, i.e.  $\delta F_{0l} = \delta F_0$ , and with scaling of the ARTP according to Eq. (3).

## Methane

The temporal evolution of global atmospheric CH<sub>4</sub> abundance,  $B_{\text{CH}_4}$  (in kg), in the emulator is given by

$$\frac{d B_{\text{CH}_4}}{dt} = -\frac{1}{\tau_{\text{CH}_4}} B_{\text{CH}_4} + E_{\text{CH}_4}, \quad (5)$$

where  $E_{\text{CH}_4}$  is the global emission rate of CH<sub>4</sub>. The atmospheric CH<sub>4</sub> half-life,  $\tau_{\text{CH}_4}$ , depends on the time scales of different loss processes,

$$\frac{1}{\tau_{\text{CH}_4}} = \frac{1}{\tau_{\text{OH}}} + \frac{1}{\tau_{\text{strat}}} + \frac{1}{\tau_{\text{soil}}} + \frac{1}{\tau_{\text{trop-Cl}}}. \quad (6)$$

The time scale for destruction of CH<sub>4</sub> by tropospheric hydroxyl (OH) radicals,  $\tau_{\text{OH}}$ , in Eq. (6) is parameterized based on annual emissions of NO<sub>x</sub> ( $E_{\text{NO}_x}$ ), CO ( $E_{\text{CO}}$ ), and VOC ( $E_{\text{VOC}}$ ), following Ehhalt et al. (2001) and Stocker et al. (2013),

$$\frac{1}{\tau_{\text{OH}}} = \frac{1}{\tau_{\text{OH}}^0} \left[ \left( \frac{B_{\text{CH}_4}}{B_{\text{CH}_4}^0} \right)^s \exp(s_{\text{NO}_x} E_{\text{NO}_x} + s_{\text{CO}} E_{\text{CO}} + s_{\text{VOC}} E_{\text{VOC}}) \right], \quad (7)$$

with the sensitivity coefficients  $s = -0.31$ ,  $s_{\text{NO}_x} = 0.0042 \text{ yr/Tg(N)}$ ,  $s_{\text{CO}} = -0.000105 \text{ yr/Tg(CO)}$ ,  $s_{\text{VOC}} = -0.000315 \text{ yr/Tg(VOC)}$ , and reference value  $B_{\text{CH}_4}^0 = 4957.74 \text{ Tg}$  (1783.36 ppb) for year 2005 (Meinshausen et al., 2017). The time scales for all loss processes are provided in Table S4.

In contrast to the original parameterization by Ehhalt et al. (2001), it is assumed that temperature-induced changes in CH<sub>4</sub> concentrations are negligible, compared to the concentration impacts of emission changes, which avoids the need for an iterative calculation of temperature changes in the emulator.

Above equations are slightly modified in order to determine responses of CH<sub>4</sub> abundance to specific emission sources, assuming that emissions from these sources are a relatively small fraction of the total emissions from all sources. In particular, the contribution of CH<sub>4</sub> emissions from a specific emission sector or region to the baseline CH<sub>4</sub> abundance is obtained using a linear decomposition of the abundances and emissions in Eq. (5), followed by integration of the resulting equation.  $\tau_{\text{OH}}$  is perturbed by reducing  $B_{\text{CH}_4}$  in Eq. (7) relative to the baseline abundance in order to account for impacts of the sectoral or regional emissions on the CH<sub>4</sub> lifetime.

Changes in CH<sub>4</sub> abundance in response to emissions of CO, NO<sub>x</sub>, or VOC from a specific emission sector or region are obtained by reducing the baseline emissions by the emissions from that source and calculating  $\tau_{\text{OH}}$  based on the reduced emissions and perturbed CH<sub>4</sub> abundance.

The radiative forcing efficiency of CH<sub>4</sub> is given by

$$A(t) = A_0 \exp\left(-\frac{t}{\tau_{\text{CH}_4}}\right),$$

with an initial radiative forcing efficiency, immediately following the pulse emission of CH<sub>4</sub>,

$$A_0 = \frac{\delta F_0}{\delta B_{\text{CH}_4}},$$

which is obtained by evaluating the sensitivity of the effective  $\text{CH}_4$  radiative forcing to a small perturbation in  $\text{CH}_4$  abundance, similar to the calculations for  $\text{CO}_2$ , assuming an efficacy of  $\epsilon = 1$ . The global mean effective  $\text{CH}_4$  radiative forcing at the top-of-atmosphere is calculated following Etminan et al. (2016), using the simulated baseline  $\text{CH}_4$  abundance and a specified  $\text{N}_2\text{O}$  abundance of 323 ppb.

$\text{CH}_4$  radiative forcings associated with emissions of  $\text{CH}_4$ ,  $\text{CO}$ ,  $\text{NO}_x$ , or  $\text{VOC}$  from specific emission sectors or regions are determined by using reduced emissions to calculate perturbed  $\text{CH}_4$  abundances, relative to total baseline emissions. Calculations with reduced emissions are performed separately, for each emitted chemical species. In order to determine the contributions of the emission sources to the baseline radiative forcing, the perturbed abundances are used to calculate radiative forcings, which are subsequently subtracted from the baseline radiative forcing.

The Absolute Global Temperature-Change Potential of  $\text{CH}_4$  (Eq. 1) is given by

$$\text{AGTP}(H) = A_0 \sum_{j=1}^2 \frac{\tau_{\text{CH}_4} c_j}{\tau_{\text{CH}_4} - d_j} \left[ \exp\left(-\frac{H}{\tau_{\text{CH}_4}}\right) - \exp\left(-\frac{H}{d_j}\right) \right]$$

and the ARTP of  $\text{CH}_4$  is given by Eq. (2), with  $\delta F_{0l} = \delta F_0$ , and scaling of the ARTP according to Eq. (3).

For analysis of the impacts of regional  $\text{CH}_4$ ,  $\text{CO}$ ,  $\text{NO}_x$ , and  $\text{VOC}$  emissions, the ARTP is linearly decomposed into contributions from regional emission sources, similar to the calculations for  $\text{CO}_2$ .

### Aerosols

Effective radiative forcings associated with interactions of aerosols with radiation, clouds and surface albedo are determined using an extension of the approach by Ghan (2013). For each one of the four latitude bands in the emulator, a series of annual mean effective radiative forcings for interactions of aerosols with radiation, clouds, and surface albedo is obtained by averaging results of equilibrated climate model simulations with specified sea surface temperatures and sea ice. Separate effective forcings are determined, corresponding to emissions of different aerosols or chemical precursor species from different sources and regions. These are obtained by perturbing the emissions (removal of sources), relative to emissions in the reference year. Subsequently, the radiative forcings are used to determine radiative forcing sensitivities  $f_p$ , where  $p$  refers to the perturbed emitted chemical species, region, or forcing process.

Simulated global aerosol radiative forcings in the emulator are comparable to results from previous multi-model based assessments (Figure S1). Uncertainties exist due to differences in reference years, emission data, and a general lack of data from ESM simulations.

Owing to the relatively short lifetime of tropospheric aerosols, the aerosol radiative forcing efficiency can be approximated by a step-function,

$$A(t) = A_0 U(\delta t_0 - t) \quad ,$$

with the Heaviside function  $U(t)$  and

$$A_0 = \frac{\epsilon f_p}{\delta t_0} .$$

This yields

$$\text{AGTP}(H) = A_0 \sum_{j=1}^2 \frac{\delta t_0 c_j}{d_j} \exp\left(-\frac{H}{d_j}\right),$$

with the approximation

$$\exp\left(\frac{\delta t_0}{d_j}\right) \approx 1 + \frac{\delta t_0}{d_j}.$$

For simulations of the interactions of sulfate aerosols with radiation, it is assumed that  $\epsilon = 1$  (Hansen et al., 2005; Richardson et al., 2019) and the ARTP (Eq. 2) is scaled according to Eq. (3). The RTP and ARTP are calculated from radiative forcings which are obtained by multiplying  $f_p$  with emissions.

The efficacies of black and organic carbon due to their interactions with radiation may differ markedly from unity (e.g. Hansen et al., 2005; Modak and Bala, 2019). These are derived from the RTP by invoking an additional constraint on the global equilibrium temperature change, by matching the global and the globally integrated regional equilibrium temperature responses, i.e.

$$\lambda \epsilon \delta F_0 = \sum_l \sum_m k_{lm} \delta F_{0l} z_l.$$

This yields  $\epsilon = 1/g$  and therefore implies that the ARTPs for black and organic carbon no longer explicitly depend on  $\epsilon$  or  $g$ , which results in the simplified expressions

$$A_0 = \frac{f_p}{\delta t_0}$$

and

$$\text{ARTP}_m(H) = \text{AGTP}(H) \left(\frac{1}{\lambda \delta F_0}\right) \text{RTP}_m.$$

Similar to the interactions of black and organic carbon with radiation, it is assumed that the efficacies of aerosols resulting from interactions with clouds and surface albedos may differ from unity, particularly for impacts of black carbon on snow albedo (Hansen et al., 2005; Flanner, 2013; Modak et al., 2016). Consequently,  $\epsilon = 1/g$  is used to represent the temperature impacts associated with interactions of aerosols with clouds and surface albedos.

### Ozone

The ARTP for tropospheric ozone is closely related to the aerosol ARTP. However, radiative forcing sensitivities could not be derived from the limited amount of data available from the 3D climate models. Gridded annual mean direct time-evolving ozone forcing maps from UKESM1 are used, which include contributions from all ozone precursors emissions and methane. These are used to determine a time series of annually varying net radiative forcings for each latitude band,  $F_l(t)$ .

By using time-evolving radiative forcings instead of emissions, the aerosol ARTP described above can be modified to approximate the regional temperature response to  $F_l(t)$ ,

$$\begin{aligned} & T_m(t + \delta t_0) - T_{0m}(t + \delta t_0) \\ &= \left(\frac{g\epsilon}{\lambda}\right) \sum_{n=0}^N U(t - t_0 - n\delta t_0) \sum_{j=1}^2 \frac{\delta t_0 c_j}{d_j} \exp\left(-\frac{t - t_0 - n\delta t_0}{d_j}\right) \sum_{l=1}^M k_{lm} F_l(t_0 + n\delta t_0), \end{aligned}$$

where  $\epsilon = 1/g$  to account for the relatively low efficacy of ozone, compared to greenhouse gases (Hansen et al., 2005).

Note that with the approach used for CH<sub>4</sub> in the emulator, emissions of VOCs, CO, and NO<sub>x</sub> affect climate via changes in the global abundance and radiative forcing of CH<sub>4</sub> in the atmosphere. While these species also affect O<sub>3</sub> radiative forcings and temperatures in the emulator, as described above, the current version of the emulator does not directly link the temperature changes to emissions of VOCs, CO, and NO<sub>x</sub>. Additional model simulations with UKESM1, or similar models, would be required to do so and therefore simulations are currently limited to the net forcing and temperature impacts of concurrently changing ozone precursor emissions.

### References

Alcamo, J., Krol, M. and Posch, M., 1995, An integrated analysis of sulfur emissions, acid deposition and climate change. *Water Air Soil Pollut.* 85, 1539–1550, <https://doi.org/10.1007/BF00477200>.

AMAP, 2015, AMAP Assessment 2015: Black carbon and ozone as Arctic climate forcers. Arctic Monitoring and Assessment Programme (AMAP), Oslo, Norway. vii + 116 pp.

AMAP, 2021, Impacts of Short-lived Climate Forcers on Arctic Climate, Air Quality, and Human Health. Summary for Policy-makers. Arctic Monitoring and Assessment Programme (AMAP), Tromsø, Norway. 20 pp.

Ban-Weiss, G. A., Cao, L., Bala, G., and Caldeira, K., 2011, Dependence of climate forcing and response on the altitude of black carbon aerosols, *Climate Dynamics*, 38, 897-911.

Boucher, O., and Reddy, M., 2008, Climate trade-off between black carbon and carbon dioxide emissions, *Energ. Policy*, 36, 193–200.

Collins, W. J., Fry, M. M., Yu, H., Fuglestedt, J. S., Shindell, D. T., and West, J. J., 2013, Global and regional temperature-change potentials for near-term climate forcers, *Atmos. Chem. Phys.*, 13, 2471–2485, <https://doi.org/10.5194/acp-13-2471-2013>.

Ehhalt, D., Prather, M., Dentener, F., Derwent, R., Dlugokencky, E., Holland, E., Isaksen, I., Katima, J., Kirchhoff, V., Matson, P., Midgley, P., Wang, M., Berntsen, T., Bey, I., Brasseur, G., Buja, L., Collins, W. J., Daniel, J., DeMore, W. B., Derek, N., Dickerson, R., Etheridge, D., Feichter, J., Fraser, P., Friedl, R., Fuglestedt, J., Gauss, M., Grenfell, L., Grüber, A., Harris, N., Hauglustaine, D., Horowitz, L., Jackman, C., Jacob, D., Jaeglé, L., Jain, A., Kanakidou, M., Karlsdottir, S., Ko, M., Kurylo, M., Lawrence, M., Logan, J. A., Manning, M., Mauzerall, D., McConnell, J., Mickley, L., Montzka, S., Müller, J. F., Olivier, J., Pickering, K., Pitari, G., Roelofs, G. J., Rogers, H., Rognerud, B., Smith, S., Solomon, S., Staehelin, J., Steele, P., Stevenson, D., Sundet, J., Thompson, A., van Weele, M., van Kuhlmann, R., Wang, Y., Weisenstein, D., Wigley, T., Wild, O., Wuebbles, D., Yantosca, R., 2001, Atmospheric chemistry and greenhouse gases, In: *Climate Change 2001: The Scientific Basis. Contribution of Working Group I to the Third Assessment Report of the Intergovernmental Panel on Climate Change* [Houghton, J.T., Ding, Y., Griggs, D. J., Noguer, M., van der Linden, P. J., Dai, X., Maskell, K., and Johnson, C. A. (eds.)]. Cambridge University Press, Cambridge, United Kingdom and New York, NY, USA, 881pp.

Etminan, M., Myhre, G., Highwood, E. J., and Shine, K. P., 2016, Radiative forcing of carbon dioxide, methane, and nitrous oxide: A significant revision of the methane radiative forcing, *Geophys. Res. Lett.*, 43, 12,614–12,623, doi:10.1002/2016GL071930.

- Flanner, M.G., 2013, Arctic climate sensitivity to local black carbon. *Journal of Geophysical Research: Atmospheres*, 118, 1840-1851.
- Foley, K. M., Napelenok, S. L., Jang, C., Phillips, S., Hubbell, B. J., and Fulcher, C. M., 2014, Two reduced form air quality modeling techniques for rapidly calculating pollutant mitigation potential across many sources, locations and precursor emission types, *Atmospheric Environment*, 98, 283–289, <https://doi.org/10.1016/j.atmosenv.2014.08.046>.
- Forster, P. M., Maycock, A. C., McKenna, C.M. et al., 2020, Latest climate models confirm need for urgent mitigation, *Nat. Clim. Chang.*, 10, 7–10, <https://doi.org/10.1038/s41558-019-0660-0>.
- Forster, P. M., Richardson, T., Maycock, A. C., Smith, C. J., Samset, B. H., Myhre, G., Andrews, T., Pincus, R., and Schulz, M., 2016, Recommendations for diagnosing effective radiative forcing from climate models for CMIP6, *J. Geophys. Res. Atmos.*, 121, 12,460–12,475, doi:10.1002/2016JD025320.
- Fuglestedt, J. S., Shine, K. P., Berntsen, T., Cook, J., Lee, D. S., Stenke, A., Skeie, R. B., Velders, G. J. M., and Waitz, I. A., 2010, Transport impacts on atmosphere and climate: Metrics, *Atmospheric Environment*, 44, 4648-4677, <https://doi.org/10.1016/j.atmosenv.2009.04.044>.
- Geoffroy, O., Saint-Martin, D., Olivié, D. J. L., Voldoire, A., Bellon, G., and Tytéca, S., 2013, Transient climate response in a two-layer energy-balance model. Part I: Analytical solution and parameter calibration using CMIP5 AOGCM experiments, *J. Climate*, 26, 1841–1857, <https://doi.org/10.1175/JCLI-D-12-00195.1>.
- Ghan, S. J., 2013, Technical note: Estimating aerosol effects on cloud radiative forcing, *Atmos. Chem. Phys.*, 13, 9971–9974, <https://doi.org/10.5194/acp-13-9971-2013>.
- Good, P., Gregory, J. M., and Lowe, J. A., 2011, A step-response simple climate model to reconstruct and interpret AOGCM projections, *Geophys. Res. Lett.*, 38, I01703, <https://doi.org/10.1029/2010GL045208>.
- Hansen, J., Sato, M., Ruedy, R., Nazarenko, L., Lacis, A., Schmidt, G. A., Russell, G., Aleinov, I., Bauer, M., Bauer, S., Bell, N., Cairns, B., Canuto, V., Chandler, M., Cheng, Y., del Genio, A., Faluvegi, G., Fleming, E., Friend, A., Hall, T., Jackman, C., Kelley, M., Klang, N., Koch, D., Lean, J., Lerner, J., Lo, K., Menon, S., Miller, R., Minnis, P., Novakov, T., Olinas, V., Perlwitz, Ja., Perlwitz, Ju., Rind, D., Romanou, A., Shindell, D., Stone, P., Sun, S., Tausnev, N., Thresher, D., Wielicki, B., Wong, T., Yao, M., and Zhang, S., 2005, Efficacy of climate forcings. *Journal of Geophysical Research: Atmospheres*, 110, D18104, doi:10.1029/2005JD005776.
- Heyes, C., Klimont, Z., Wagner, F., and Amann, M., 2011, Extension of the GAINS model to include short-lived climate forcers. IIASA Report. IIASA, Laxenburg, Austria.
- Li, J., Yang, W., Wang, Z., Chen, H., Hu, B., Li, J., Sun, Y., and Huang, Y., 2014, A modeling study of source–receptor relationships in atmospheric particulate matter over Northeast Asia, *Atmospheric Environment*, 91, 40–51, <https://doi.org/10.1016/j.atmosenv.2014.03.027>.
- Liu, Y., Hong, Y., Fan, Q., Wang, X., Chan, P., Chen, X., Lai, A., Wang, M., and Chen, X., 2017, Source-receptor relationships for PM<sub>2.5</sub> during typical pollution episodes in the Pearl River Delta city cluster, China, *Sci. Total Environ.*, 596–597, 194–206, <https://doi.org/10.1016/j.scitotenv.2017.03.255>.

- Meehl, G. A., C. A. Senior, V. Eyring, G. Flato, J.-F. Lamarque, R. J. Stouffer, K. E. Taylor, M. Schlund, 2020, Context for interpreting equilibrium climate sensitivity and transient climate response from the CMIP6 Earth system models. *Sci. Adv.* **6**, eaba1981.
- Meinshausen, M., Raper, S., and Wigley, T., 2011, Emulating coupled atmosphere-ocean and carbon cycle models with a simpler model, MAGICC6 – Part 1: Model description and calibration, *Atmos. Chem. Phys.*, **11**, 1417–1456, <https://doi.org/10.5194/acp-11-1417-2011>.
- Meinshausen, M., Vogel, E., Nauels, A., Lorbacher, K., Meinshausen, N., Etheridge, D. M., Fraser, P. J., Montzka, S. A., Rayner, P. J., Trudinger, C. M., Krummel, P. B., Beyerle, U., Canadell, J. G., Daniel, J. S., Enting, I. G., Law, R. M., Lunder, C. R., O'Doherty, S., Prinn, R. G., Reimann, S., Rubino, M., Velders, G. J. M., Vollmer, M. K., Wang, R. H. J., and Weiss, R., 2017, Historical greenhouse gas concentrations for climate modelling (CMIP6), *Geosci. Model Dev.*, **10**, 2057–2116, <https://doi.org/10.5194/gmd-10-2057-2017>.
- Millar, R. J., Nicholls, Z. R., Friedlingstein, P., and Allen, M. R., 2017, A modified impulse-response representation of the global near-surface air temperature and atmospheric concentration response to carbon dioxide emissions, *Atmos. Chem. Phys.*, **17**, 7213–7228, <https://doi.org/10.5194/acp-17-7213-2017>.
- Modak, A. and G. Bala, 2019, Efficacy of black carbon aerosols: the role of shortwave cloud feedback, *Environ. Res. Lett.*, **14**, 084029, <https://doi.org/10.1088/1748-9326/ab21e7>.
- Modak, A., G. Bala, L. Cao, and K. Caldeira, 2016, Why must a solar forcing be larger than a CO<sub>2</sub> forcing to cause the same global mean surface temperature change? *Environ. Res. Lett.*, **11**, 044013, <https://doi.org/10.1088/1748-9326/11/4/044013>.
- Myhre, G., Shindell, D., Breon, F.-M., Collins, W., Fuglestad, J., Huang, J., Koch, D., Lamarque, J.-F., Lee, D., Mendoza, B., Nakajima, T., Robock, A., Stephens, G., Takemura, T., and Zhang, H., 2013, Anthropogenic and natural radiative forcing: Supplementary material, in: *Climate Change 2013: The Physical Science Basis. Contribution of Working Group I to the Fifth Assessment Report of the Intergovernmental Panel on Climate Change*, edited by: Stocker, T. F., Qin, D., Plattner, G.-K., Tignor, M., Allen, S. K., Boschung, J., Nauels, A., Xia, Y., Bex, V., and Midgley, P. M.
- Nijssen, F. J. M. M., Cox, P. M., and Williamson, M. S., 2020, Emergent constraints on transient climate response (TCR) and equilibrium climate sensitivity (ECS) from historical warming in CMIP5 and CMIP6 models, *Earth Syst. Dynam.*, **11**, 737–750, <https://doi.org/10.5194/esd-11-737-2020>.
- Porter, P. S., Rao, S. T., Hogrefe, C., and Mathur, R., 2017, A reduced form model for ozone based on two decades of CMAQ simulations for the continental United States, *Atmos. Pollut. Res.*, **8**, 275–284, <https://doi.org/10.1016/j.apr.2016.09.005>.
- Prather, M. J., Holmes, C. D., and Hsu, J., 2012, Reactive greenhouse gas scenarios: Systematic exploration of uncertainties and the role of atmospheric chemistry, *Geophys. Res. Lett.*, **39**, doi:10.1029/2012GL051440.
- Richardson, T. B., Forster, P. M., Smith, C. J., Maycock, A. C., Wood, T., Andrews, T., et al., 2019, Efficacy of climate forcings in PDRMIP models. *Journal of Geophysical Research: Atmospheres*, **124**, 12,824–12,844. <https://doi.org/10.1029/2019JD030581>.
- Roe, G., 2009, Feedbacks, timescales, and seeing red, *Annual Review of Earth and Planetary Sciences*, **37**, 93–115, <https://doi.org/10.1146/annurev.earth.061008.134734>.

- Sand, M., Berntsen, T., Kay, J. E., Lamarque, J. F., Seland, Ø., and Kirkevåg, A., 2013, The arctic response to remote and local forcing of black carbon, *Atmos. Chem. and Phys.*, 13, 211-224.
- Schmidt, G. A., et al., 2006, Present-day atmospheric simulations using GISS ModelE: Comparison to in situ, satellite, and reanalysis data, *J. Climate*, 19, 153–192, <https://doi.org/10.1175/JCLI3612.1>.
- Sherwood, S., Webb, M. J., Annan, J. D., Armour, K. C., Forster, P. M., Hargreaves, J. C., et al., 2020, An assessment of Earth's climate sensitivity using multiple lines of evidence, *Reviews of Geophysics*, 58, e2019RG000678. <https://doi.org/10.1029/2019RG000678>.
- Shindell, D., 2012, Evaluation of the absolute regional temperature potential, *Atmos. Chem. Phys.*, 12, 7995–8007, doi:10.5194/acp-12-7955-2012.
- Shindell, D., and Faluvegi, G., 2009, Climate response to regional radiative forcing during the twentieth century, *Nature Geosci.*, 2, 294–300, doi:10.1038/NGEO473.
- Shindell, D., and Faluvegi, G., 2010, The net climate impact of coal-fired power plant emissions, *Atmos. Chem. Phys.*, 10, 3247–3260, <https://doi.org/10.5194/acp-10-3247-2010>.
- Shine, K. P., Fuglestvedt, J. S., Hailemariam, K., Stuber, N., 2005, Alternatives to the global warming potential for comparing climate impacts of emissions of greenhouse gases, *Climatic Change*, 68, 281–302.
- Smith, C. J., Forster, P. M., Allen, M., Leach, N., Millar, R. J., Passerello, G. A., and Regayre, L. A., 2018, FAIR v1.3: a simple emissions-based impulse response and carbon cycle model, *Geosci. Model Dev.*, 11, 2273–2297, <https://doi.org/10.5194/gmd-11-2273-2018>.
- Stocker, T. F., Qin, D., Plattner, G.-K., Tignor, M., Allen, S. K., Boschung, J., Nauels, A., Xia, Y., Bex, V., and Midgley, P., eds., 2013, *Climate change 2013: The physical science basis. Contribution of Working Group I to the fifth assessment report of the Intergovernmental Panel on Climate Change*, Cambridge University Press, Cambridge, United Kingdom and New York, NY, USA, 1535 pp.
- Thornhill, G. D., Collins, W. J., Kramer, R. J., Olivie, D., Skeie, R. B., O'Connor, F. M., Abraham, N. L., Checa-Garcia, R., Bauer, S. E., Deushi, M., Emmons, L. K., Forster, P. M., Horowitz, L. W., Johnson, B., Keeble, J., Lamarque, J.-F., Michou, M., Mills, M. J., Mulcahy, J. P., Myhre, G., Nabat, P., Naik, V., Oshima, N., Schulz, M., Smith, C. J., Takemura, T., Tilmes, S., Wu, T., Zeng, G., and Zhang, J., 2021, Effective radiative forcing from emissions of reactive gases and aerosols – a multi-model comparison, *Atmos. Chem. Phys.*, 21, 853–874, <https://doi.org/10.5194/acp-21-853-2021>.
- Tsutsui, J., 2020, Diagnosing transient response to CO<sub>2</sub> forcing in coupled atmosphere-ocean model experiments using a climate model emulator, *Geophys. Res. Lett.*, 47, e2019GL085844, <https://doi.org/10.1029/2019GL085844>.
- Van Dingenen, R., Dentener, F., Crippa, M., Leitao, J., Marmer, E., Rao, S., Solazzo, E., and Valentini, L., 2018, TM5-FASST: a global atmospheric source–receptor model for rapid impact analysis of emission changes on air quality and short-lived climate pollutants, *Atmos. Chem. Phys.*, 18, 16173–16211, <https://doi.org/10.5194/acp-18-16173-2018>.
- Voulgarakis, A., Naik, V., Lamarque, J.-F., Shindell, D. T., Young, P. J., Prather, M. J., Wild, O., Field, R. D., Bergmann, D., Cameron-Smith, P., Cionni, I., Collins, W. J., Dalsøren, S. B., Doherty, R. M., Eyring, V., Faluvegi, G., Folberth, G. A., Horowitz, L. W., Josse, B., MacKenzie, I. A., Nagashima, T., Plummer, D. A., Righi, M., Rumbold, S. T., Stevenson, D. S., Strode, S. A., Sudo, K., Szopa, S., and

Zeng, G., 2013, Analysis of present day and future OH and methane lifetime in the ACCMIP simulations, *Atmos. Chem. Phys.*, 13, 2563–2587, doi:10.5194/acp-13-2563-2013.

Yang, Y., Smith, S. J., Wang, H., Mills, C. M., and Rasch, P. J., 2019, Variability, timescales, and nonlinearity in climate responses to black carbon emissions, *Atmos. Chem. Phys.*, 19, 2405–2420, <https://doi.org/10.5194/acp-19-2405-2019>.

Zelinka, M. D., Myers, T. A., McCoy, D. T., Po-Chedley, S., Caldwell, P. M., Ceppi, P., et al., 2020, Causes of higher climate sensitivity in CMIP6 models, *Geophys. Res. Lett.*, 47, e2019GL085782. <https://doi.org/10.1029/2019GL085782>.

CO <sub>2</sub> , CH <sub>4</sub> , SO <sub>4</sub> ,		Forcing region				Ref.
OC (RAD)		60°N - 90°N	28°N - 60°N	28°S - 28°S	90°S - 28°S	
	60°N - 90°N	0.31	0.17	0.16	0.06	1
Response	28°N - 60°N	0.06	0.24	0.17	0.07	1
Region	28°S - 28°S	0.02	0.10	0.24	0.09	1
	90°S - 28°S	0.00	0.02	0.05	0.19	1
BC (RAD)		Forcing region				Ref.
		60°N - 90°N	28°N - 60°N	28°S - 28°S	90°S - 28°S	
	60°N - 90°N	variable	0.15	0.31	0.06	2
Response	28°N - 60°N	0.08	0.14	0.24	0.07	1
Region	28°S - 28°S	0.02	0.07	0.17	0.09	1
	90°S - 28°S	0.00	0.02	0.06	0.19	1
O <sub>3</sub> (RAD)		Forcing region				Ref.
		60°N - 90°N	28°N - 60°N	28°S - 28°S	90°S - 28°S	
	60°N - 90°N	0.07	0.05	0.13	0.06	1
Response	28°N - 60°N	0.06	0.20	0.15	0.07	1
region	28°S - 28°S	0.02	0.09	0.26	0.09	1
	90°S - 28°S	-0.03	-0.06	0.13	0.19	1
BC, OC, SO <sub>4</sub>		Forcing region				Ref.
(ALB)		60°N - 90°N	28°N - 60°N	28°S - 28°S	90°S - 28°S	
	60°N - 90°N	0.49	0.15	0.31	0.06	2
Response	28°N - 60°N	0.08	0.14	0.24	0.07	2
region	28°S - 28°S	0.02	0.07	0.17	0.09	2
	90°S - 28°S	0.00	0.02	0.06	0.19	2
BC, OC, SO <sub>4</sub>		Forcing region				Ref.
(CLD)		60°N - 90°N	28°N - 60°N	28°S - 28°S	90°S - 28°S	
	60°N - 90°N	0.31	0.17	0.16	0.06	2
Response	28°N - 60°N	0.06	0.24	0.17	0.07	2
region	28°S - 28°S	0.02	0.10	0.24	0.09	2
	90°S - 28°S	0.00	0.02	0.05	0.19	2

**Table S1:** Regional temperature response coefficients in K (W m<sup>-2</sup>)-1, for unit forcing from changes in climate forcer concentrations and different forcing processes (RAD: interactions with radiation in the atmosphere, ALB: interactions with surface albedo, CLD: interactions with clouds) in the emulator. References (last column): 1: Collins et al. (2013); 2: see text.

Layer $y$	Pressure range (hPa)	$\hat{k}_y$ (K (W m <sup>-2</sup> ) <sup>-1</sup> )
1	10 - 20	-0.337
2	20 - 30	-0.328
3	30 - 50	-0.315
4	50 - 70	-0.298
5	70 - 100	-0.276
6	100 - 150	-0.241
7	150 - 200	-0.197
8	200 - 250	-0.153
9	250 - 300	-0.110
10	300 - 400	-0.044
11	400 - 500	0.043
12	500 - 600	0.131
13	600 - 700	0.218
14	700 - 850	0.438
15	850 - 925	0.757
16	925 - 1000	1.157

**Table S2:** Arctic black carbon temperature response coefficients.

Loss process	Time scale		Emission fraction	
	Notation	Value (yr)	Notation	Value
Geological re-absorption	$\tau_{\text{CO}_2,1}$	$1 \cdot 10^6$	$a_1$	0.2173
Deep ocean invasion/equilibration	$\tau_{\text{CO}_2,2}$	394.4	$a_2$	0.2240
Biospheric uptake/ocean thermocline invasion	$\tau_{\text{CO}_2,3}$	36.54	$a_3$	0.2824
Rapid biospheric uptake/ocean mixed-layer invasion	$\tau_{\text{CO}_2,4}$	4.304	$a_4$	0.2763

**Table S3:** Time scales of CO<sub>2</sub> loss processes in the emulator, following Millar et al. (2017).

Loss process	Notation	Time scale (yr)
Destruction of CH <sub>4</sub> by tropospheric OH	$\tau_{\text{OH}}^0$	11.17
Loss in the stratosphere	$\tau_{\text{strat}}$	120
Uptake by soils	$\tau_{\text{soil}}$	150
Reaction with tropospheric chlorine	$\tau_{\text{trop-Cl}}$	200

**Table S4:** Time scales of CH<sub>4</sub> loss processes in the emulator, following Prather et al. (2012) and Voulgarakis et al. (2013).

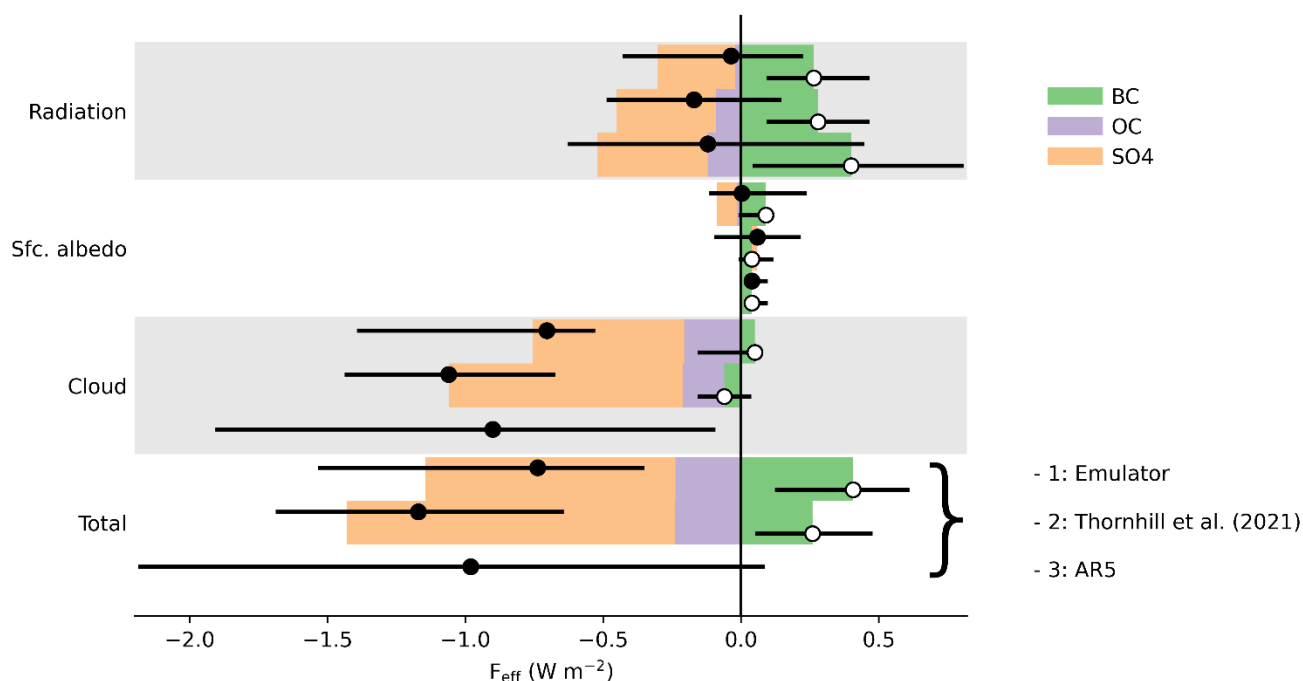


**Figure S1:** Comparison of global mean aerosol effective radiative forcings in the emulator (first bar) with results from CMIP6 multi-model assessment (middle bar; Thornhill et al., 2021), and 5<sup>th</sup> IPCC assessment report, based on CMIP5 data (bottom bar; Stocker et al., 2013), as indicated on the right. Each one of the three estimates refers to a different reference year for present-day: 2015 (top bar), 2014 (middle bar), and 2005 (bottom), but all forcing estimates are relative to pre-industrial conditions in 1850. Black bullets and whiskers refer to net radiative forcings and confidence intervals for each emitted species. White circles refer to the contributions of black carbon to net radiative forcings, with confidence intervals (whiskers). Contributions of different aerosol species (sulfate, organic and black carbon) are shown, where available (colours, as indicated on the right). Global sulfur emissions in the AMAP inventory used in the emulator are low compared to emissions used by CMIP5 and CMIP6, which partly explains differences in sulfate radiative forcings (see the summary of emission data sets).